Check for updates

Detailed kinetic model for combustion of NH₃/H₂ blends

Yu-Chi Kao, [ab] Anna C. Doner, [a] Timo T. Pekkanen, [a] Chuangchuang Cao, [a] Sunkyu Shin, [a] Alon Grinberg Dana, [c] Yi-Pei Li [b] and William H. Green [*a]

Ammonia is a promising zero-carbon fuel for industrial and transport applications, but its combustion is hindered by low reactivity, flame instabilities, incomplete oxidation, and the formation of nitrogen oxides. Accurate and detailed kinetic models are critical for designing optimal burners and engines. Despite numerous mechanisms published in recent years, large discrepancies remain between model predictions and experimental data, particularly for NO$_x$ species. In this work, we compile updated thermochemical and kinetic parameters for ammonia combustion from critically evaluated literature sources and high-level *ab initio* calculations, minimizing reliance on estimated parameters. A new detailed kinetic mechanism was generated using the reaction mechanism generator (RMG). For six key pressure-dependent reactions, recently developed bath-gas mixture rules and temperature-dependent third-body efficiencies were applied to improve the treatment of composition effects. The resulting mechanism was validated against experimental laminar-burning velocities, ignition-delay times, flow-reactor species profiles, and jet-stirred-reactor data, and compared with several recent literature mechanisms. Without any empirical rate-coefficient adjustments, the model reproduces many experimental observations with good overall agreement, while remaining discrepancies highlight persistent uncertainties in nitrogen-oxide chemistry. As no parameters were tuned to reproduce specific experimental targets, we expect the model to extrapolate well to conditions where experimental data are limited.

1 Introduction

Ammonia (NH$_3$) has emerged as a promising carbon-free alternative to conventional fuels for industrial and transport applications owing to its high power-to-fuel-to-power efficiency,[1] a large-scale distribution infrastructure that is already in place, a high octane rating, and potential for large-scale production from sustainable sources.[2–4] Despite these advantages, its practical use as a fuel poses several challenges. Ammonia is inherently difficult to ignite and sustain in combustion due to its low reactivity, which often results in unstable flames and unacceptable NH$_3$ emissions.[5] Additionally, high-temperature oxidation can promote the formation of pollutants such as nitrogen oxides (NO$_x$). To achieve stable and clean combustion, ammonia is frequently co-fired with more reactive fuels such as hydrocarbons or H$_2$,[6] but this approach introduces additional design complexity. Accurate and predictive kinetic mechanisms

are therefore needed as input for computational fluid dynamics (CFD) simulations, which are used to design clean and efficient ammonia-combustion reactors.

Although numerous NH$_3$ combustion mechanisms have been developed, recent review articles[6–10] highlight that these models often disagree with one another and exhibit systematic discrepancies relative to experimental results. The disagreement between models stems from the use of inconsistent sets of reactions, as well as kinetic and thermochemical parameters for key species and reactions. Discrepancies with experimental data may arise from missing key reactions (mechanism-truncation error) and how pressure dependence is treated in multi-component gas mixtures. Most existing mechanisms essentially neglect the bath-gas-composition dependence of pressure-dependent reactions or approximate it using the classical mixture rule. As demonstrated by Burke and co-workers,[11–13] and more recently by Stagni and Dinelli,[14] treating the composition effect has a non-negligible effect on modeling targets such as laminar-burning velocities (LBVs) and ignition-delay times (IDTs). The classical mixture rule works well when the important reactions are close to the low-pressure limit—which is the case for many measurements of modeling targets—but in the fall-off region the

^{a} *Department of Chemical Engineering, Massachusetts Institute of Technology, Cambridge, MA 02139, USA. E-mail: whgreen@mit.edu*

^{b} *Department of Chemical Engineering, National Taiwan University, Taipei, Taiwan*

^{c} *Wolfson Department of Chemical Engineering and Grand Technion Energy Program, Technion – Israel Institute of Technology, Haifa 3200003, Israel*

This journal is © the Owner Societies 2026

Phys. Chem. Chem. Phys., 2026, **28**, 6411–6424 | **6411**

error introduced by utilizing the classical mixture rule can exceed typical uncertainties of pure-bath-gas rate coefficients.

In this work, we address these shortcomings by:

(1) Updating the reaction mechanism generator (RMG) database[15,16] with thermochemical and kinetic parameters recommended by Grinberg Dana and co-workers.[7,17,18]

(2) Constructing a mechanism with RMG to reduce mechanism-truncation error.

(3) Refining RMG-estimated rate coefficients with values obtained from *ab initio* calculations.

(4) Applying an improved mixture rule developed by the Burke group for key pressure-dependent reactions,[13] and utilizing temperature-dependent third-body efficiencies determined by Jasper.[19]

The resulting mechanism is comprehensive and can be used to identify the kinetically important reactions over a wide range of temperatures, pressures, and equivalence ratios relevant to ammonia and hydrogen combustion. Once validated, it can be systematically reduced using model-reduction techniques[20] to enable its use in CFD simulations.

RMG generates kinetic mechanisms by iteratively selecting species and reactions from a hypothesized "edge" and promoting them to the "core" mechanism by analysing computed instantaneous fluxes. Both edge and core species and reactions require thermochemical and kinetic parameters, for which RMG uses literature values when available and group-additivity or rate-rule estimates when not. In this work, we made a conscious effort to minimize the number of reactions for which RMG needs to rely on such estimates. While this automated approach ensures broad coverage, uncertainties in estimates and the occasional generation of "non-physical" molecules that have valid Lewis structures but are not a minimum on any potential-energy surface (PES) can degrade model accuracy.[21] To mitigate these issues, we carefully screened the generated species, removed non-physical candidates, and recalculated thermochemical parameters for valid species. This procedure enhances the fidelity of the RMG-generated mechanism.

To further assess performance, we compare the RMG-generated mechanism developed in this work with state-of-the-art literature mechanisms. Szanthoffer *et al.*[6] and Girhe *et al.*[9] recently ranked and evaluated NH$_3$/H$_2$ combustion mechanisms according to their agreement with experimental data, identifying both strengths and weaknesses for each mechanism. Here, we compare our mechanism with five of the best-performing mechanisms,[8,22–25] as well as with experimental results for pure NH$_3$, pure H$_2$, and blended NH$_3$/H$_2$ mixtures.

2 Computational and modeling methods

2.1 Rate-coefficient calculations

A detailed description of the rate-coefficient calculations is provided in the SI, and only a brief summary of the employed

methods and programs is given here. Depending on the reaction, geometry optimizations and frequency analyses were performed at the ωB97X-D/def2-QZVP, UHF-CCSD(T)/aug-cc-pVTZ, CASPT2/aug-cc-pVTZ, and ωB97X-D/def2-TZVP levels of theory.[26–28] Single-point energies were evaluated at the CASPT2/CBS (complete basis set), CCSD(T)/CBS, and CCSD(T)-F12/cc-pVTZ-F12 levels of theory. Molpro,[29–31] Gaussian 16,[32] and ORCA[33] software packages were utilized to execute these calculations. In some cases, we used the automated rate calculator (ARC),[34] interfaced with Gaussian and Molpro to facilitate the quantum-chemistry calculations. CCSDT(Q) corrections were computed with the MRCC program.[35,36] Specifically, high-level electronic structure calculations were performed for the O(^{3}P) + HNO, ^{2}HO$_2$ + ^{3}NH, and H + ^{2}H$_2$NO reaction systems, as detailed in the SI. Phenomenological rate coefficients were determined with ARC, Arkane,[37] and MESMER 7.1.[38] For barrierless reactions, we employed both Gaussrate[39] and a custom implementation of the Flexible-Transition-State Theory (FTST) method of Robertson *et al.*;[40] this code is provided in the SI. The VRC-TST/Gaussrate output files are also given in the SI.

2.2 Thermochemistry calculations

For each edge species generated by RMG, geometries were optimized at the ωB97X-D/def2-TZVPD level of theory. Initial guess geometries were obtained by selecting the lowest-energy conformer from a UFF force-field search performed with RDKit.[41] Species with geometries that match the intended graph representation were considered physical. For species that failed this initial step, RDKit was used to generate ten additional conformers, each of which was optimized at the ωB97X-D/def2-TZVPD level of theory. If at least one of these geometries matched the intended graph representation, the species was retained; otherwise, the species was deemed non-physical. In total, 61 species were identified as non-physical. We confirmed that these species do not impact core rate coefficients and forbade these structures during mechanism generation.

For the remaining species, thermochemical parameters were calculated using ARC. Conformer searches were performed initially at the ωB97X-D/def2-SVP level of theory, with final geometry optimization, frequency, and hindered-rotor calculations performed at the ωB97X-D/def2-TZVP level of theory. Single-point energies were obtained at the DLPNO-CCSD(T)-F12/cc-pVTZ-F12 level of theory. Atomization energy corrections and Petersson-type bond additivity corrections were applied following the Wu *et al.* protocol.[42]

2.3 Mechanism generation with RMG

The mechanism was generated under 24 conditions that covered the ranges 700–1900 K, 1.0–100.0 bar, equivalence ratios of ϕ = 0.25–2.0, and NH$_3$/H$_2$ blend ratios ranging from 100%/0% to 0%/100%. Pressure-dependent rate coefficients were estimated using the modified strong collision method with a grain size of 2.1 kJ mol^{-1}, over a temperature range of 500–2000 K and a pressure range of 0.1–100 bar. The complete RMG input file, including further details such as selected tolerances, is provided in the SI.

6412 | *Phys. Chem. Chem. Phys.*, 2026, **28**, 6411–6424

This journal is © the Owner Societies 2026

2.4 Modeling methods and analysis

The generated mechanism for the blended oxidation of NH_3 and H_2 was tested against a range of experimental data using simulations performed with Cantera 3.1.[43] IDTs and hydroxyl time histories from shock-tube experiments were compared with results from ideal zero-dimensional (0D) transient simulations assuming a step-function change in temperature at $t = 0$, and the experimental temperature values as reported. LBVs were determined using one-dimensional (1D) simulations including multi-component transport and thermal diffusion. These results were compared with experimental LBV data extrapolated to zero strain by the experimental group. Finally, the model's species-concentration predictions were tested against concentration-time profiles from jet-stirred reactor (JSR) and flow reactor (FR) experiments. The FR simulations were performed as a 1D, constant-pressure reactor with the measured centreline temperature profiles as inputs.

As shown below, for many observables the various models yield similar values, both among themselves and relative to the predictions of our new mechanisms. In some cases, the deviations between the model predictions and experimental data fall within the reported experimental uncertainties. It should be noted that all simulations were performed under ideal-reactor assumptions, and that the experimental analyses also involve simplifying assumptions. Future studies would benefit greatly from the inclusion of well-defined confidence intervals for both experimental data and model predictions, which would enable a more quantitative assessment of model–experiment consistency.
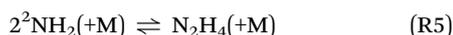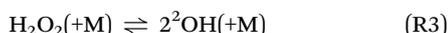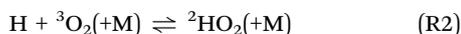
The rate coefficients of complex-forming reactions depend on both pressure and bath-gas composition. However, as mentioned in the Introduction, the composition dependence is typically neglected by assuming a pure N_2 bath gas or by approximating it using the classical mixture rule. The classical mixture rule provides only a crude approximation and can

Table 1 Modified Arrhenius parameters for the reactions added or updated in our mechanism. The superscripted number before each open-shell species' formula is its spin multiplicity

No.	Reaction	A (cm³ mol⁻¹ s⁻¹)	n	E_a (kJ mol⁻¹)	Ref.
Bimolecular abstraction reactions					
1	$^4N + {}^2HO_2 \rightarrow {}^3NH + {}^3O_2$	1.82×10^{-27}	9.81	60.5	17
2	$^2NO + {}^2HO_2 \rightarrow HNO + {}^3O_2$	1.19×10^{-5}	5.06	29.9	17
3	$^2H_2NO + {}^2HO_2 \rightarrow NH_3O + {}^3O_2$	1.40×10^{-5}	4.53	8.1	17
4	$^2NNH + {}^2HO_2 \rightarrow N_2H_2 + {}^3O_2$	6.25×10^{-5}	4.57	2.2	17
5	$^2HO_2 + {}^2NH_2 \rightarrow H_2O_2 + {}^3NH$	1.97×10^{-5}	5.23	34.2	17
6	$^2HO_2 + NH_3 \rightarrow H_2O_2 + {}^2NH_2$	4.44×10^{-1}	4.00	75.5	17
7	$^2HO_2 + {}^2N_2H_3 \rightarrow H_2O_2 + {}^3H_2NN$	2.79×10^{-3}	4.00	7.9	17
8	$^2HO_2 + HNO_2 \rightarrow H_2O_2 + {}^2NO_2$	2.49×10^{-3}	4.52	0.2	17
9	$^2HO_2 + N_2H_2 \rightarrow H_2O_2 + {}^2NNH$	7.79×10^{-1}	3.96	-0.6	17
10	$HNO + {}^2HO_2 \rightarrow {}^2HNOH + {}^3O_2$	3.08×10^{0}	2.98	2.4	17
11	$H + HNO \rightarrow H_2 + {}^2NO$	1.66×10^{10}	1.18	1.87	45
12	$^2OH + HNO \rightarrow H2O + {}^2NO$	1.20×10^{9}	1.19	1.40	46
13	$^4N + {}^3O_2 \rightarrow {}^2NO + O(^3P)$	5.90×10^{9}	1.01	6.28	47
14	$^4N + {}^2OH \rightarrow {}^2NO + {}^2H$	1.08×10^{14}	-0.20	0.0	47
15	$H + {}^2H_2NO \rightarrow H_2 + HNO$	9.60×10^{8}	1.50	6.97	pw (RMG estimate)
16	$^2NO + {}^2H_2NO \rightarrow 2HNO$	1.77×10^{-2}	4.04	84.66	pw
17	$^3O_2 + {}^3H_2NN \rightarrow {}^2HO_2 + {}^2NNH$	1.16×10^{-1}	4.05	22.0	pw
18	$HON + {}^2HO_2 \rightarrow {}^2HNOH + {}^3O_2$	7.18×10^{-2}	4.13	0.5	pw
19	$^2HO_2 + {}^2HNOH \rightarrow H_2O_2 + HON$	2.56×10^{-5}	4.86	14.0	pw
20	$^4N + {}^2HNOH \rightarrow {}^3NH + HON$	7.77×10^{-2}	4.22	33.5	pw
21	$^3NH + {}^2HNOH \rightarrow {}^2NH_2 + HON$	1.18×10^{1}	3.65	11.0	pw
22	$^2NO + {}^3H_2NN \rightarrow HNO + {}^2NNH$	1.15×10^{1}	3.25	18.9	pw
23	$HON + N_2H_2 \rightarrow {}^2HNOH + {}^2NNH$	7.12×10^{-7}	5.50	21.1	pw
24	$2{}^2HNOH \rightarrow NH_2OH + HON$	3.55×10^{-6}	5.15	20.7	pw
25	$HON + HONO \rightarrow {}^2HNOH + {}^2NO_2$	8.07×10^{-12}	6.62	59.9	pw
26	$H + NH_2OOH \rightarrow H_2 + {}^2NH_2OO$	3.75×10^{2}	3.35	37.9	pw
27	$^2HO_2 + NH_2OOH \rightarrow H_2O_2 + {}^2NH_2OO$	2.37×10^{-10}	6.27	44.4	pw
28	$^2NH_2 + NH_2OOH \rightarrow NH_3 + {}^2NH_2OO$	4.29×10^{-5}	4.69	15.9	pw
29	$^3NH + NH_2OOH \rightarrow {}^2NH_2 + {}^2NH_2OO$	9.21×10^{-7}	5.51	36.8	pw
30	$^2NH_2OO + NH_2OH \rightarrow NH_2OOH + {}^2HNOH$	1.31×10^{-9}	5.96	32.6	pw
31	$O(^3P) + HNO \rightarrow {}^2OH + {}^2NO$	7.24×10^{15}	-1.04	0.0644	pw
		2.84×10^{12}	0.322	4.68	
32	$^3NH + {}^2HO_2 \rightarrow {}^2NH_2 + {}^3O_2$	2.40×10^{-26}	11.1	75.0	pw
		4.34×10^{3}	2.95	-5.79	
Well-skipping bimolecular reactions (low-pressure limit)					
33	$^2NH_2 + O(^3P) \rightarrow (NH_2O/NHOH) \rightarrow {}^3NH + {}^2OH$	3.09×10^{3}	2.84	-11.63	45
34	$^2NH_2 + O(^3P) \rightarrow (NH_2O/NHOH) \rightarrow {}^2NO + H_2$	2.38×10^{12}	0.112	-1.452	45
35	$^2NH_2 + O(^3P) \rightarrow (NH_2O/NHOH) \rightarrow HNO + {}^2H$	2.78×10^{13}	-0.065	-0.787	45
36	$H + {}^2H_2NO \rightarrow (NH_2OH/NH_3O) \rightarrow H2 + HNO$	8.69×10^{3}	2.60	4.71	pw
37	$H + {}^2H_2NO \rightarrow (NH_2OH/NH_3O) \rightarrow {}^2NH_2 + {}^2OH$	3.704×10^{13}	0.15	8.13	pw
38	$^2HO_2 + {}^3NH \rightarrow ({}^2HNOOH) \rightarrow {}^2OH + HNO$	2.60×10^{7}	1.81	-10.5	pw
39	$^2HO_2 + {}^3NH \rightarrow ({}^2HNOOH/{}^2H_2NOO) \rightarrow {}^3O_2 + {}^2NH_2$	2.22×10^{27}	-5.36	25.6	pw
40	$^2HO_2 + {}^3NH \rightarrow ({}^2HNOOH/{}^2H_2NOO) \rightarrow O(^3P) + {}^2H_2NO$	1.24×10^{8}	0.386	110.7	pw

This journal is © the Owner Societies 2026

Phys. Chem. Chem. Phys., 2026, **28**, 6411–6424 | **6413**

introduce errors of up to a factor of two or so when reactions are not close to the low- or high-pressure limit. In addition, practical implementations of the rule in modeling software also often require the user to specify temperature-independent efficiencies, when in fact these efficiencies can exhibit strong temperature dependence.[19] Recently, the Burke group has developed improved mixture rules to address some of the shortcomings of the classical mixture rule,[11–13] and the implementation of their work in Cantera 3.1 allows the user to specify temperature-dependent third-body efficiencies. To improve our treatment of composition dependence, we applied the linear-mixture rule in reduced pressure (LMR-R) for the following key reactions:
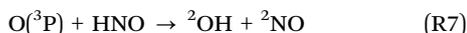
$$H + {}^2OH(+M) \rightleftharpoons H_2O(+M) \tag{R1}$$

$$H + {}^3O_2(+M) \rightleftharpoons {}^2HO_2(+M) \tag{R2}$$

$$H_2O_2(+M) \rightleftharpoons 2{}^2OH(+M) \tag{R3}$$

$$NH_3(+M) \rightleftharpoons H + {}^2NH_2(+M) \tag{R4}$$

$$2{}^2NH_2(+M) \rightleftharpoons N_2H_4(+M) \tag{R5}$$

$$HNO(+M) \rightleftharpoons H + {}^2NO(+M). \tag{R6}$$

For the third-body efficiencies, we utilized the results of Jasper.[19]

3 Results and discussion

3.1 Rate coefficients

Table 1 lists the reactions added into the RMG-database, as well as their modified Arrhenius parameters. For most of these rate coefficients, there are no experimental measurements, but the

$$O({}^3P) + HNO \rightarrow {}^2OH + {}^2NO \tag{R7}$$

reaction is one exception. We show in Fig. 1 the computed rate coefficient together with the experimental data measured by

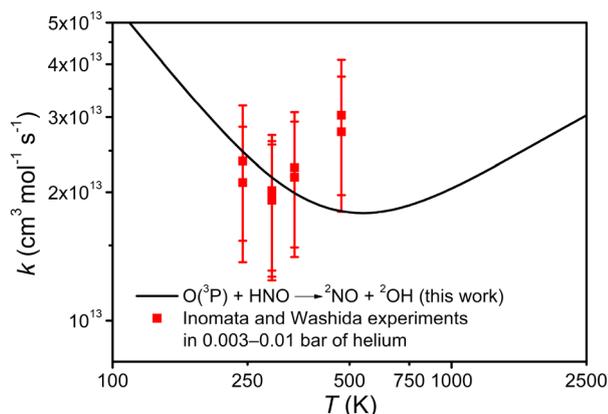Inomata and Washida.[44] To obtain better agreement with direct experimental measurement, we lowered the energy of the rate-determining saddle-point by 2.4 kJ mol^{-1}, which is well within computational uncertainties. Master-equation simulations revealed that the recombination reaction to form HNO$_2$ followed by decomposition to H + ^{2}NO$_2$ is never competitive with (R7).

Consistent with the findings of Monge-Palacios *et al.*,[8] additional computational and experimental studies—particularly for reactions such as (R7) and other processes involving nitroxyl radical chemistry—are needed to further refine kinetic models and represent an important direction for future research. Master-equation simulations for the

$$H + {}^2H_2NO \rightarrow (NH_2OH/NH_3O) \rightarrow H_2 + HNO \tag{R8a}$$

$$H + {}^2H_2NO \rightarrow (NH_2OH/NH_3O) \rightarrow {}^2NH_2 + {}^2OH \tag{R8b}$$

and

$${}^2HO_2 + {}^3NH \rightarrow (HNOOH/H_2NOO) \rightarrow {}^2OH + HNO \tag{R9a}$$

$${}^2HO_2 + {}^3NH \rightarrow (HNOOH/H_2NOO) \rightarrow {}^3O_2 + {}^2NH_2 \tag{R9b}$$

$${}^2HO_2 + {}^3NH \rightarrow (HNOOH/H_2NOO) \rightarrow O({}^3P) + {}^2H_2NO \tag{R9c}$$

reactions revealed that the initially formed adducts never stabilize, and that these reactions are at the low-pressure limit under all practical conditions ($p \leq 100$ bar). For (R8), channel (R8b) dominates over nearly the entire temperature range considered, while the direct-abstraction reaction H + ^{2}H$_2$NO $\rightarrow$ H$_2$ + HNO becomes competitive at higher temperatures. A similar behaviour is observed for (R9): among the well-skipping channels, only (R9a) is kinetically significant under most conditions, with the competing direct abstraction pathway forming ^{2}NH$_2$ + ^{3}O$_2$ gaining importance at higher temperatures. The results are depicted graphically in Fig. 2 and 3.

For the bimolecular abstraction reactions tabulated in Table 1, the temperature dependencies of the rate coefficients are depicted in Fig. 4.

3.2 Thermochemistry calculations

Fig. 5 shows a parity plot of the standard enthalpy of formation ($\Delta_f H_{298\,K}^{\theta}$) estimated by RMG *via* group-additivity or hydrogen-bond-increment (HBI) correction to quantum chemistry calculations according to Pang *et al.*[48] for 137 edge species that passed screening. While most estimates agree within 100 kJ mol^{-1}, deviations of several hundred kJ mol^{-1} are observed for some species, particularly those obtained from group-additivity methods. The updated thermochemical data were added to the RMG-database and then subsequently used for mechanism generation in this work.

3.3 Summary of RMG mechanism

The RMG generated mechanism consists of 53 species and 704 reactions. The corresponding mechanism files in both Cantera and Chemkin formats are provided in the SI. All thermochemical parameters are taken from high-level calculations or recommendations by Grinberg Dana *et al.*[7] As shown in
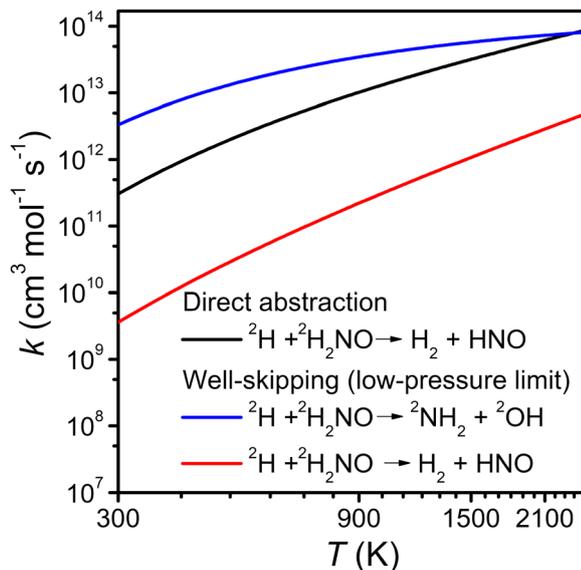

Fig. 1 Computed rate coefficient for the O(^{3}P) + HNO $\rightarrow$ ^{2}OH + ^{2}NO reactions shown together with the experimental determination by Inomata and Washida.[44] The submerged saddle-point for this reaction was lowered by 2.4 kJ mol^{-1} to obtain better agreement with experiment.

6414 | *Phys. Chem. Chem. Phys.*, 2026, **28**, 6411–6424

This journal is © the Owner Societies 2026

Fig. 2 Computed rate coefficients for the well-skipping H + ^2H_2NO → (NH$_2$OH/NH$_3$O) → H$_2$ + HNO and H + ^2H_2NO → (NH$_2$OH/NH$_3$O) → $_2$NH$_2$ + ^2OH reactions shown together with the direct-abstraction reaction H + ^2H_2NO → H$_2$ + HNO. The first two reactions were found to still be at the low-pressure limit at 100 bar.
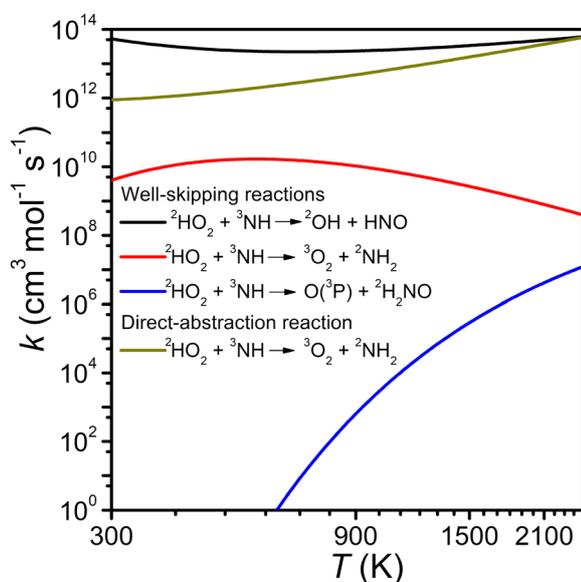
Fig. 3 Computed rate coefficients for the well-skipping $^2HO_2$ + ^3NH → (HNOOH) → ^2OH + HNO, HO$_2$ + ^3NH → (HNOOH/H$_2$NOO) → $^3O_2$ + $^2NH_2$ and $^2HO_2$ + ^3NH → (HNOOH/H$_2$NOO) → O(^3P) + 2H$_2$NO. The reactions were found to still be at the low-pressure limit at 100 bar. Only the ^2OH + HNO forming channel is relevant in practice.

Fig. 6, the kinetic parameters for 359 reactions are sourced from the literature (RMG-database), and 92 are estimated by RMG *via* the pressure-dependent network. The remaining rate coefficients are determined using estimation rules, primarily for disproportionation (*n* = 194) and hydrogen abstraction (*n* = 59) reactions. Although both Cantera and Chemkin input files are included for completeness, LMR-R is currently implemented

only in Cantera; therefore, all simulations presented in this work were performed using Cantera.

3.4 Model validation

Fundamental combustion experiments of ammonia and ammonia/hydrogen mixtures provide valuable insights into how global reactivity of the fuel mixtures and the generation and destruction of chemical species of interest depend on temperature (*T*), pressure (*p*), equivalence ratio (*ϕ*), blending ratio, *etc*. The experimental data also serve as validation targets for the development of an accurate and predictive combustion mechanism. The performance of the developed mechanism is validated against a comprehensive set of experimental data for the combustion of pure H$_2$, pure NH$_3$, and NH$_3$/H$_2$ mixtures with varying H$_2$ content. This section presents a selection of these validation results, focusing on key combustion targets: IDTs, LBVs, and species profiles measured in JSRs and FRs. To assess the importance of improved mixture rules, we present two versions of our mechanism; one that implements the classical mixture rule with temperature-independent third-body efficiencies (RMG) and another that implements LMR-R with temperature-dependent third-body efficiencies (RMG_Burke). Because the objective of this work is to isolate and assess the impact of updated N–H–O kinetics on NH$_3$/H$_2$ oxidation, our primary benchmarking set focuses on mechanisms specifically designed for N/H/O chemistry. Recent quantitative evaluations[9] consistently rank NUIG_2023, KAUST_2021, KAUST_2023, and POLIMI/CRECK_2023 among the best-performing NH$_3$/H$_2$ mechanisms across IDTs, LBVs, and NH$_3$/H$_2$ speciation datasets. These mechanisms also avoid optimized C$_1$-C$_3$ hydrocarbon subsets, which lie outside the scope of the present N–H–O–only study. For completeness, additional NH$_3$–H$_2$–C$_1$ mechanisms (*e.g.*, NUIG_2023;[49] Shrestha_2025;[50] Zhang_2023[24]) are compared in the SI, but all mechanistic conclusions in this work are based on the N/H/O benchmarking set. Furthermore, we compare the performance of these two models (RMG and RMG_Burke) with five recently developed state-of-the-art mechanisms.[8,22–25]

3.4.1 Ignition delay time. IDTs measured in shock tubes are essential for validating the intermediate- and high-temperature oxidation mechanisms of ammonia-based fuels. The performance of the current mechanism was evaluated by comparing predicted IDTs against two comprehensive experimental datasets for pure NH$_3$ and NH$_3$/H$_2$ mixtures. Mathieu and Petersen[51] measured IDTs of NH$_3$/O$_2$/Ar mixtures over a wide range of conditions, covering 1560–2455 K, pressures of approximately 1.4, 11, and 30 atm, and equivalence ratios of 0.5, 1.0, and 2.0. More recently, Chen *et al.*[52] investigated the influence of H$_2$ addition on the autoignition of NH$_3$ in stoichiometric NH$_3$/H$_2$/O$_2$/Ar mixtures. Their measurements span 1020–1945 K, pressures of 1.2 and 10 atm, and H$_2$ mole fractions from 0% to 70%. These datasets provide crucial targets for evaluating the high-temperature performance of our mechanism.

Fig. 7 compares model-predicted IDTs with shock-tube measurements for pure NH$_3$ at pressures from 1.4 to 30 atm. Across all conditions considered, the deviations between model

This journal is © the Owner Societies 2026

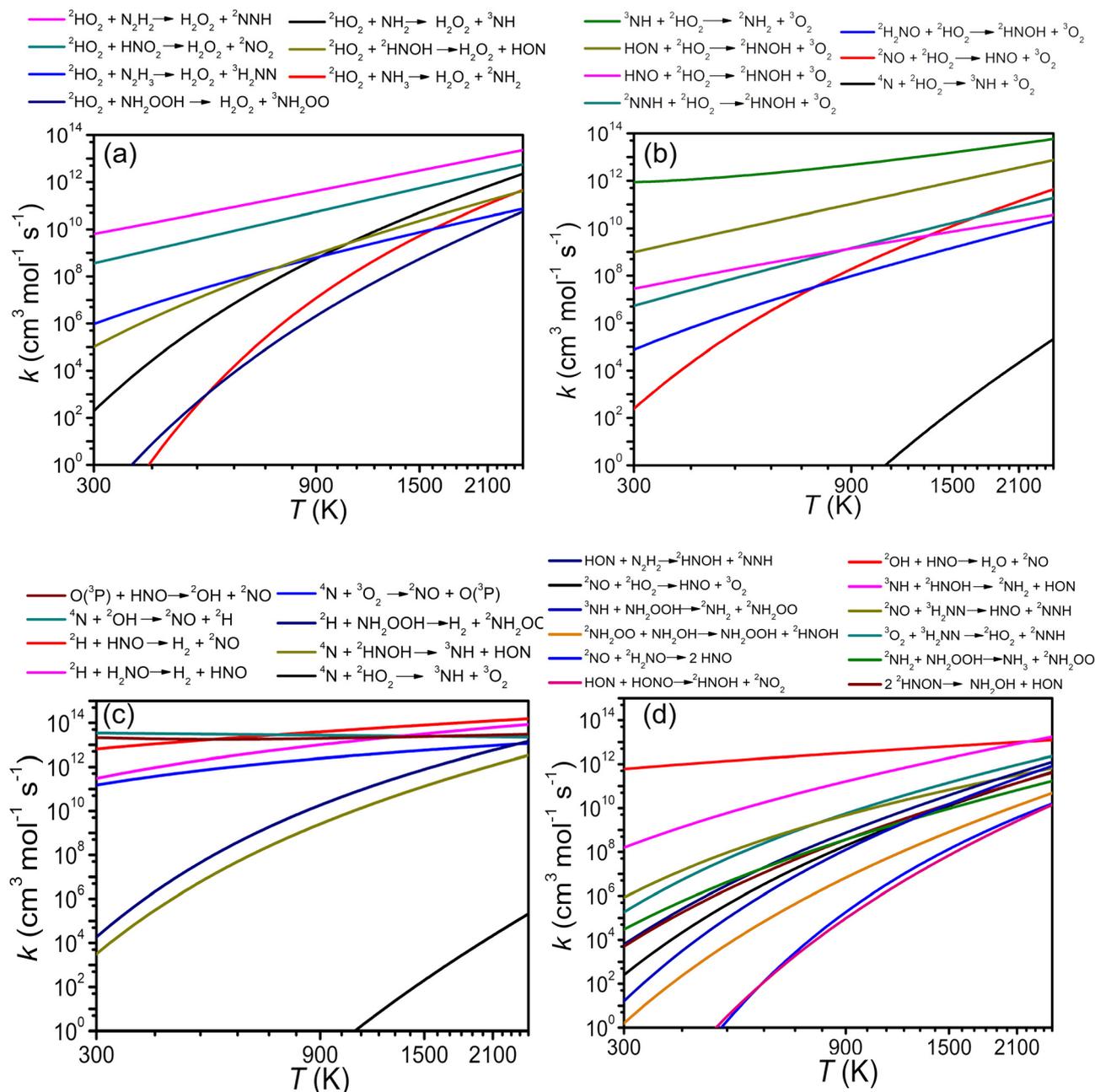*Phys. Chem. Chem. Phys.*, 2026, **28**, 6411–6424 | **6415**

Fig. 4 The temperature dependencies of the H-abstraction rate coefficients updated or computed in this work. Panels (a)–(d) show different subsets of reactions for clarity, as the full set would be overly crowded in a single plot.

predictions and experimental measurements remain within a factor of two. At 1.4 atm, the comparison shows a clear dependence on both temperature range and experimental dataset. For the lower-temperature measurements of Chen *et al.* (1800–2000 K),[52] all mechanisms underpredict the measured IDTs. Among them, only the RMG and RMG_Burke mechanisms reproduce the data within approximately 20%, which is comparable to the reported experimental uncertainty; whereas the KAUST mechanisms exhibit substantially larger deviations, with mean discrepancies exceeding 40%. In contrast, for the higher-temperature measurements of Mathieu

et al. (>2300 K),[51] all mechanisms reproduce the experimental IDTs within similar bounds. At 11 atm, a similar dataset-dependent trend is observed. When compared against the Chen *et al.* measurements, only the RMG, RMG_Burke, and NUIG mechanisms show good agreement with the experimental data, while the KAUST mechanisms exhibit larger deviations, typically exceeding a factor of about 1.5. At 30 atm, the inter-model spread increases modestly. The CRECK_2023 and KAUST_2021 mechanisms provide the closest overall agreement with the Mathieu *et al.* data. Overall, these results indicate that while all modern mechanisms reproduce pure-NH_3 ignition delays
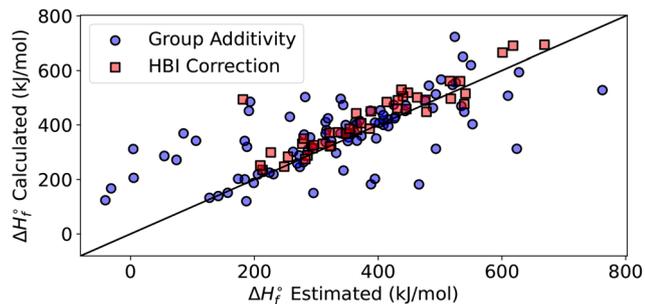
6416 | *Phys. Chem. Chem. Phys.*, 2026, **28**, 6411–6424

This journal is © the Owner Societies 2026

Fig. 5 Standard enthalpies of formation ($\Delta_f H^{\theta}_{298\,K}$) calculated at DLPNO-CCSD(T)-F12/cc-pVTZ-F12//ωB97X-D/def2-TZVP are compared to estimates by RMG,[15,16] including group additivity (blue circles) and HBI corrections[48] (red squares).
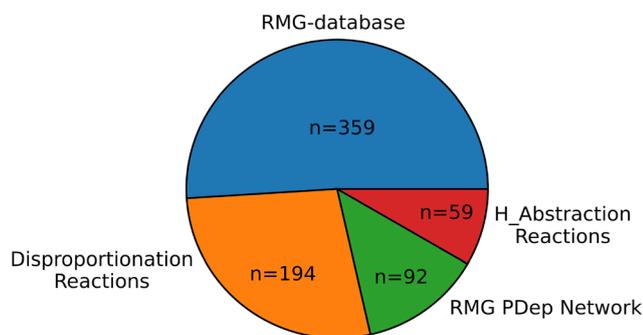

Fig. 6 Sources of rate-coefficient parameters in the current RMG core mechanism.

across the examined conditions, the relative performance depends sensitively on pressure, temperature range, and the experimental dataset used for validation.

The model's performance for the ignition of NH_3/H_2 mixtures was evaluated against the experimental data of Chen *et al.*,[52] as shown in Fig. 8. At low pressure (1.2 atm), nearly all mechanisms reproduce the experimental ignition delays with good accuracy, with typical deviations of less than 20%, which fall within the experimental uncertainty reported by Chen *et al.*, indicating limited sensitivity to the choice of mechanism under these conditions. Among the mechanisms compared, RMG, RMG_Burke, and NUIG_2024 mechanisms perform slightly better, although differences between models remain modest at this pressure. At higher pressure (10 atm), the spread among mechanisms increases, and nearly all mechanisms underpredict the experimental ignition delay times. The largest discrepancies are observed for the 30% NH_3/70% H_2 mixture, for which the CRECK_2023 mechanism significantly underpredicts the IDTs, with deviations exceeding a factor of two. In contrast, RMG and RMG_Burke mechanisms provide comparatively better agreement under these conditions. This shared tendency among mechanisms to underpredict ignition delays at elevated pressures suggests that the coupled NH_3/H_2 kinetics under high-pressure, H_2-rich conditions are not yet fully captured. In particular, pressure-

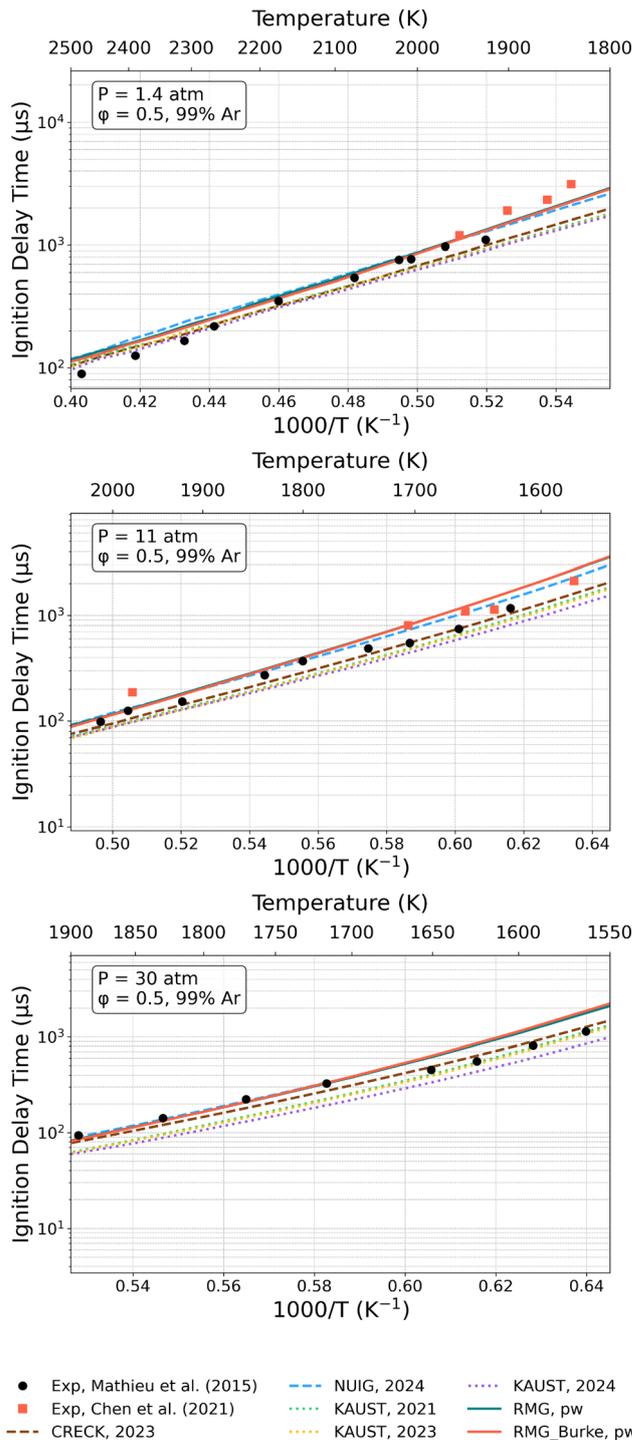**Fig. 7** The NH_3 IDT predictions of the current RMG mechanisms and recently developed literature mechanism[8,22–25] compared with experimental data.[51,52]

dependent competition between NH_3– and H_2–derived radical pathways may require further refinement. These discrepancies highlight the need for improved high-pressure rate coefficients and a more complete treatment of pressure- and temperature-dependent reaction channels in NH_3/H_2 combustion mechanisms.
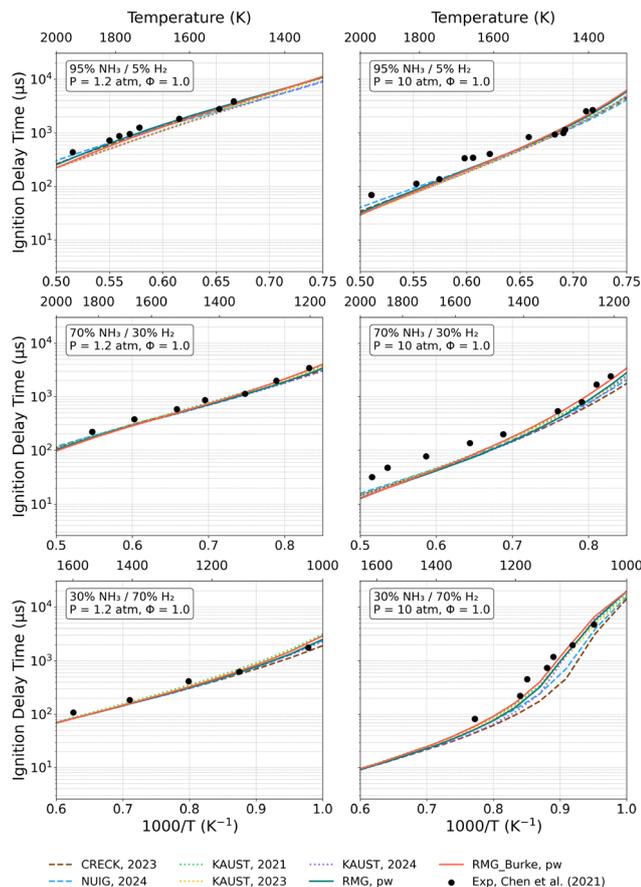
Fig. 8 The NH$_3$/H$_2$ IDT predictions of the current RMG mechanisms and recently developed literature mechanism[8,22–25] compared with experimental data.[52]

3.4.2 Laminar–Burning velocity. LBV is a key target to test a model's rate-coefficient parametrisations at high temperatures, particularly for reactions involving hydrogen atoms. It is a

fundamental property of a fuel–oxidizer mixture, describing the speed at which a smooth, unstretched flame front propagates through a stationary unburned gas. LBVs are measured using a variety of experimental techniques, typically on strained flames, and then extrapolated to zero-strain values for ease of comparison. When multiple datasets under similar conditions are available, it allows for some assessment of the uncertainty in the measurements. For alternative fuels like ammonia and ammonia–hydrogen mixtures, accurate LBV data are vital for designing and optimizing combustion systems for power generation. Recent experimental work by Lhuillier *et al.*[52] provides LBVs of NH$_3$/H$_2$ mixtures at atmospheric pressure, covering variations in unburned gas temperature, hydrogen fraction, and equivalence ratio (ϕ). These data serve as a comprehensive benchmark for evaluating kinetic mechanisms and exploring the chemical interactions that govern flame propagation.

Fig. 9 compares experimental and model-predicted LBVs for pure H$_2$, pure NH$_3$, and NH$_3$/H$_2$ blends with air at atmospheric pressure under different unburned gas temperatures. For pure H$_2$ flames, the simulations show excellent agreement with experimental data under lean and near-stoichiometric conditions ($\phi < 1.5$). Hydrogen flames exhibit very high reactivity, with a peak LBV approaching 300 cm s^{-1} in the fuel-rich region ($\phi \approx 1.8$). At richer conditions ($\phi > 1.5$), some discrepancies between models emerge. The experimental data measured by different groups often differ by 10% or more, sometimes exceeding the discrepancies between the model predictions, likely due to systematic errors associated with varying experimental techniques. For example, Pareja *et al.*,[53] using the particle tracking velocimetry (PTV) method, report higher flame speeds, whereas the prediction by Aung,[54] employing the spherical bomb technique, obtains slightly lower values. These differences are largely attributable to methodological differences: PTV captures local burning velocities in non-stretched
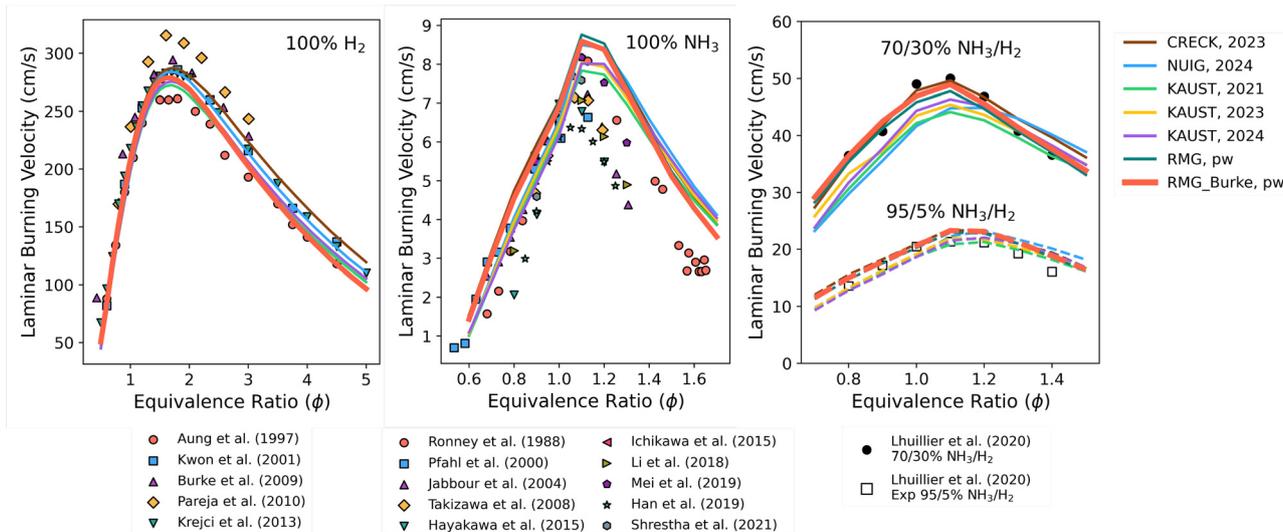

Fig. 9 The NH$_3$/H$_2$ LBV predictions of the current RMG mechanisms and recently developed literature mechanisms[8,22–25] compared with experimental data for pure H$_2$,[53–57] pure NH$_3$,[58–67] and NH$_3$/H$_2$ mixtures.[68]

6418 | *Phys. Chem. Chem. Phys.*, 2026, **28**, 6411–6424

This journal is © the Owner Societies 2026

flame regions but may be affected by flame curvature, while the spherical bomb approach measures unsteady flame propagation over short durations, potentially underestimating the LBV. Despite these methodological differences, all mechanisms and experimental datasets show consistent trends, and the theoretical predictions reproduce the high reactivity and peak location of pure hydrogen flames with good accuracy.

In contrast, the LBV of pure NH_3 flames is substantially lower than that of hydrogen, with values typically under 10 cm s^{-1}, reflecting the intrinsic difficulty of sustaining ammonia flames. The weakness of these flames likely contributes to the relatively large experimental scatter reported in the literature, particularly under atmospheric conditions, where uncertainties of 15–20% are common.[65] The peak LBV occurs consistently at a slightly fuel-rich equivalence ratio ($\phi \approx 1.1$) across both experimental datasets and numerical predictions. Most mechanisms accurately capture the flame speed under lean and near-stoichiometric conditions ($\phi \leq 1.0$), but they systematically overestimate LBVs in the fuel-rich regime ($\phi > 1.0$), in agreement with earlier comparisons showing that "most numerical simulations overpredict when compared with experimental results" for NH_3 flames.[61] More recent evaluations have reached similar conclusions, reporting that under rich combustion conditions most mechanisms substantially overpredict the LBVs.[69] In the present comparison, differences among mechanisms become more pronounced at rich equivalence ratios, although no single model consistently outperforms the others across the full range of conditions examined. These observations highlight the persistent challenges of modeling ammonia combustion, in which the NH_x radical chemistry plays a central role in controlling flame propagation.

Blending hydrogen with ammonia substantially increases the LBV, improving flame stability and making the mixture more suitable for practical energy applications. However, experimental measurements of LBVs for NH_3/H_2 blends remain limited; for example, all data shown in the third panel of Fig. 9 were measured by a single research group.[68] For a 70% NH_3/30% H_2 mixture, the measured peak flame velocity occurs at a fuel-rich equivalence ratio of $\phi \approx 1.1$, and all mechanisms considered here reproduce both the peak location and magnitude with good accuracy. Quantitatively, the deviations between model predictions and experimental measurements are small for this blend, with mean absolute errors below 10%. Among the mechanisms evaluated, RMG_Burke and RMG mechanisms yield the smallest deviations for the 70% NH_3/30% H_2 case, with mean discrepancies of less than three percent. Also, the good performance of CRECK_2023 can be attributed primarily to its slightly adjusted H_2/O_2 core kinetics, particularly the key chain-branching step $^3O_2 + H \rightleftharpoons O(^3P) + {}^2OH$, for which the pre-exponential factor was increased relative to the originally evaluated value. In addition, CRECK_2023 employs an empirically optimized treatment of third-body effects in reactions such as $H + {}^2OH\ (+M) \rightleftharpoons H_2O\ (+M)$, which modifies the balance between radical-branching and radical-termination pathways. The combined effect of these adjustments leads to an overall increase in the predicted flame-propagation rate and enables

accurate reproduction of the non-linear increase in laminar burning velocity with hydrogen fraction reported by Lhuillier et al.[68]

In contrast, RMG and RMG_Burke mechanisms were constructed strictly from first-principles and evaluated literature data, without any empirical tuning of rate coefficients to improve agreement with experimental data. For the 95% NH_3/5% H_2 mixture, both RMG and RMG_Burke mechanisms tend to predict slightly higher LBVs than measured. For pure NH_3 flames, the standard RMG mechanism predicts marginally higher LBVs than RMG_Burke near stoichiometric conditions, whereas for the 70% NH_3/30% H_2 mixture the opposite trend is observed, with RMG_Burke predicting slightly higher LBVs than RMG in the same equivalence-ratio range.

In the LBV simulations, as well as most of the other simulations, utilizing LMR-R and temperature-dependent third-body efficiencies over the classical mixture rule and temperature-independent efficiencies only had a marginal effect on the predicted modeling target. This finding is expected, as the reactions treated with the Burke rules (R1–R6) are close to the low-pressure limit under the conditions of the simulations, and linear-Burke mixture rule reduces to the classical mixture-rule both at the low- and high-pressure limits. Still, incorporating the Burke mixture rule for a general-purpose mechanism is worthwhile because it provides a more accurate treatment of the composition dependence in the fall-off region. We show in Fig. 10 how the LMR-R and classical treatments predict different rate-coefficient values for (R2) at elevated pressures.

3.4.3 Oxidation in a jet-stirred reactor. JSR experiments provide valuable benchmark data for validating kinetic mechanisms under well-mixed and steady operating conditions. For ammonia systems, speciation data from JSR experiments are particularly important, since the selectivity toward nitrogen-containing products (^2NO, N_2O) strongly influences pollutant formation. In this study, our predictions are compared with the species concentration measurements obtained in the JSR experiments of Osipova et al.[70] for pure NH_3, and Zhang et al.[23] for NH_3/H_2 mixtures under lean and stoichiometric conditions (equivalence ratios of 0.25 and 1.0) at atmospheric pressure over the temperature range 800–1280 K. Fourier-transform infrared (FTIR) spectroscopy provided quantitative data for major species (NH_3, H_2O, ^2NO, N_2O), although homonuclear species such as N_2 and H_2 were not reported.

For pure NH_3 oxidation at $\phi = 1.0$ (Fig. 11), all mechanisms reproduce the primary features of the speciation profiles: NH_3 consumption and the formation of H_2O and ^2NO are captured with good fidelity across the investigated temperature range. The experimental onset temperature for NH_3 consumption is closely matched by RMG, RMG_Burke, and NUIG_2024, with $T_{onset} \approx 1250$ K. These three mechanisms also show the best agreement for H_2O, while all mechanisms qualitatively capture the overall trend of ^2NO formation. In the experiments,[71] H_2 is observed as a transient intermediate during NH_3 oxidation, exhibiting a pronounced peak of approximately 50 ppm near 1470 K. The RMG_Burke mechanism predicts an H_2 peak of about 62 ppm at 1473 K, in close agreement with the measured

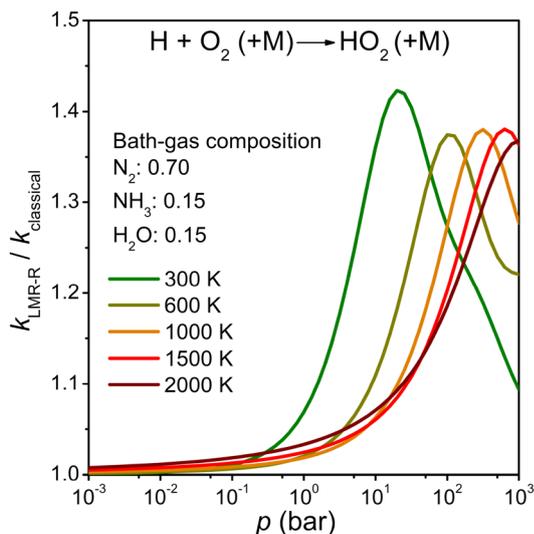This journal is © the Owner Societies 2026

Phys. Chem. Chem. Phys., 2026, **28**, 6411–6424 | **6419**

Fig. 10 The ratio of the LMR-R and classical mixture-rule H + ^{3}O$_2$ (+M) → ^{2}HO$_2$ (+M) rate coefficients plotted as a function of pressure at selected temperatures and at a constant composition of N$_2$: 0.70, NH$_3$: 0.15, and H$_2$O: 0.15.

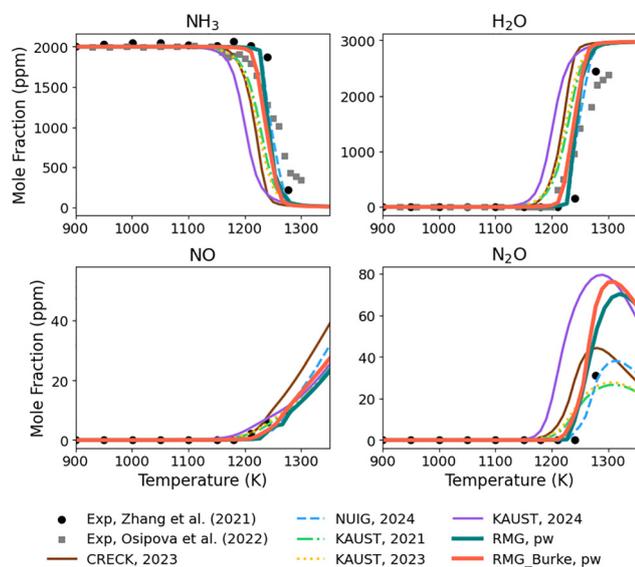**Fig. 11** RMG-generated mechanism and representative literature mechanisms[8,22–25] comparisons against species profiles in JSR oxidation of pure NH$_3$.[23,70]

value, whereas the standard RMG mechanism underpredicts this peak, yielding approximately 28 ppm at the same temperature. The NUIG_2024 mechanism predicts a comparable peak magnitude (about 36 ppm) at a similar temperature. In contrast, the KAUST mechanisms predict substantially higher H$_2$ peak concentrations (exceeding 100 ppm) and shift the peak to slightly lower temperatures (around 1420 K). The Stagni (2020) mechanism does not reproduce a pronounced H$_2$ peak, with predicted H$_2$ concentrations remaining below 10 ppm over the entire temperature range. The largest discrepancies–both

among different models and between models and experiments–are observed for N$_2$O. Among the mechanisms, NUIG_2024 better reproduces the observed onset than the other mechanisms. However, as the data extend only to ≈1280 K, and there is only one data point with a significant N$_2$O, it is difficult to draw conclusive judgments regarding the relative accuracy of the mechanisms.

For NH$_3$/H$_2$ blends at ϕ = 0.25 (Fig. 12), the onset of reactivity shifts to lower temperatures, with fuel consumption occurring more gradually than in the pure NH$_3$ case. Additional RMG and RMG_Burke comparisons across different NH$_3$/H$_2$ blending ratios are provided in the SI. Among the mechanisms evaluated, NUIG_2024 provides the closest overall agreement for the NH$_3$, H$_2$O, and NO mole-fraction profiles under these conditions. For NO, most mechanisms overpredict the onset of formation, and the largest deviations occur for N$_2$O, where only KAUST_2021, KAUST_2023, and NUIG_2024 match the peak N$_2$O mole fraction within a factor of two. For both pure NH$_3$ and NH$_3$/H$_2$, KAUST_2024 consistently predicts earlier transitions in all four major species, systematically overestimating reactivity. Overall, the NUIG_2024 mechanism achieves the best balance among the tested models but relies on multiple targeted rate adjustments to reproduce the experiment. In contrast, the RMG-based mechanisms retain *ab initio* or evaluated literature parameters without fitting to the present experimental data, leading to slightly larger deviations while maintaining consistent predictive behavior across different conditions.

It is noteworthy that KAUST_2024 predicts higher N$_2$O yields than KAUST_2023 under oxygen-lean conditions (1–10%), mainly due to employing 50% higher rate coefficient for the ^{3}NH + ^{2}NO → N$_2$O + ^{2}H reaction. In contrast, at higher O$_2$ concentrations, N$_2$O formation proceeds *via* ^{2}NH$_2$ + ^{2}NO$_2$ →

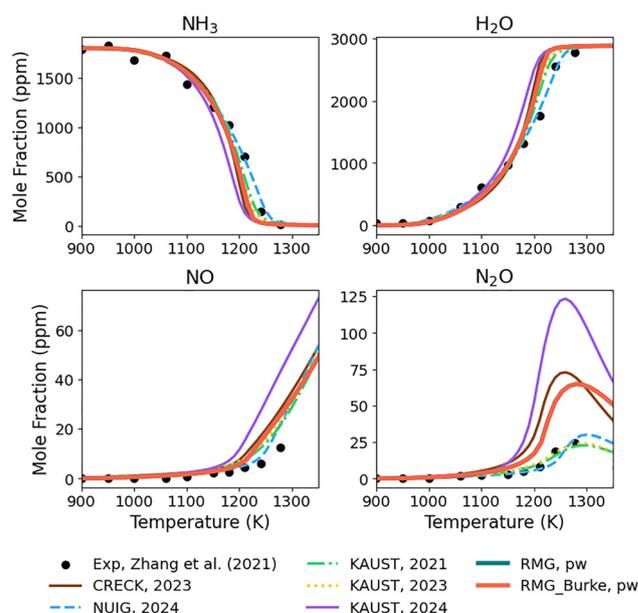**Fig. 12** RMG-generated mechanism and representative literature mechanisms[8,22–25] comparisons against species profiles in JSR oxidation of 90% NH$_3$/10% H$_2$ mixture.[23]

6420 | *Phys. Chem. Chem. Phys.*, 2026, **28**, 6411–6424

This journal is © the Owner Societies 2026

$N_2O + H_2O$, for which KAUST_2024 adopts a rate coefficient about half that of KAUST_2023, resulting in lower predicted N_2O yields. N_2O yields are sensitive to several reaction pathways, with different pathways dominating at different conditions. Accurate N_2O predictions over a wide range of reaction conditions will require very accurate determinations of several different rate coefficients.

3.4.4 Oxidation in a flow reactor. FR experiments provide critical data on the intermediate-temperature oxidation behaviour of pure NH_3 and NH_3/H_2 mixtures under short residence times (≈ 0.05 s). In this work, FR simulations were performed using a plug-flow reactor (PFR) model with temperature profiles imposed according to measurements from thermocouples.

Fig. 13, compares simulated and experimental species mole fractions for two fuel-lean oxidations in inert gas, one using pure NH_3 and the other using a $1:1$ NH_3/H_2 mixture, alongside predictions by literature mechanisms.[8,22–25,71] Our kinetic mechanisms effectively reproduce reactant consumption (NH_3, O_2, H_2) and the formation of major combustion products (N_2, H_2O). Across all conditions, the largest discrepancies are observed for [2]NO, which is generally overestimated by most mechanisms under flow-reactor conditions. Among the models considered, KAUST_2024 provides the closest agreement with the measured NO profiles, predicting systematically lower NO concentrations. This behavior reflects differences in the treatment of key NO-forming and NO-consuming reactions (reactions 13–14 in Table 1), which have a strong influence on NO_x

chemistry under these conditions. Similar trends were also observed in the JSR comparisons discussed earlier, indicating that the formation and destruction pathways of NO_x remain a key source of uncertainty in ammonia combustion modeling.

Despite these discrepancies in nitrogen-oxide chemistry, several modern mechanisms—including the RMG-based models developed in this work—reproduce the major species profiles and key combustion performance metrics, such as IDT and LBVs reasonably well. However, most models overpredict formation of the important pollutant [2]NO by a factor of 2 or more in some experiments, and many models also similarly mispredict the strong greenhouse gas N_2O. In addition, most models significantly overpredict the flame speed of rich ammonia flames. Some of these discrepancies may arise from experimental uncertainties or from the use of idealized reactor assumptions, which do not perfectly replicate the actual experimental conditions.

The RMG_Burke provides fairly good performance across the range of conditions, even though none of its parameters were adjusted to fit any of the data shown here. The NUIG_2024 achieves slightly better quantitative agreement through selective rate tuning, particularly in reproducing the experimental temperature dependence of NO_x formation. In contrast, the standard RMG-generated mechanism tends to predict earlier reactivity for most conditions, particularly at higher hydrogen fractions. Additional comparisons between the RMG and RMG_Burke mechanisms across various NH_3/H_2 blending ratios are provided in the SI.
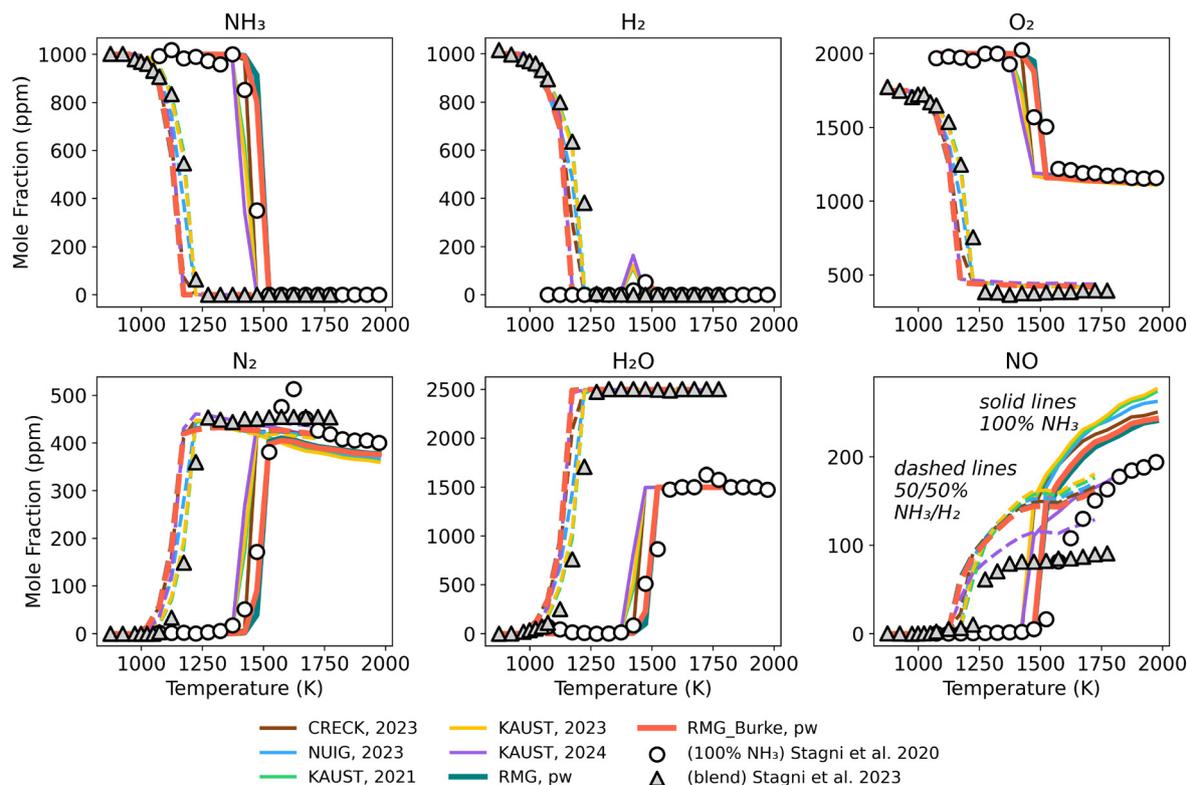

Fig. 13 Comparisons of RMG-generated mechanisms and representative literature mechanisms[8,22–25] against experimental species profiles in Flow Reactor oxidations; pure NH_3[71] (solid line) and 50%NH_3/50%H_2 mixture[22] (dashed line).

This journal is © the Owner Societies 2026

Phys. Chem. Chem. Phys., 2026, **28**, 6411–6424 | **6421**

4 Conclusions

In this work, we developed a new detailed combustion mechanism for NH_3/H_2 blends using RMG. Thermochemical and kinetic parameters were updated with the best available literature values or obtained from high-level quantum-chemical calculations when such data were unavailable. For six key reactions, the linear mixture rule in reduced pressure developed by the Burke group were implemented to better treat bath-gas–composition effects on the rate coefficients. Unlike many existing NH_3/H_2 mechanisms, the present model incorporates updated *ab initio* NH_x/O/H kinetics together with composition-dependent pressure effects and is constructed entirely without parameter tuning.

Beyond improved model performance, this work provides several advances in the mechanistic understanding of NH_3 oxidation chemistry. New *ab initio* rate coefficients are reported for previously uncertain or missing reactions that govern key NO_x-forming pathways, revealing temperature dependences that differ qualitatively from those adopted in existing mechanisms.

Extensive validation against IDTs, LBVs, and species profiles in FR and JSR shows that the new RMG_Burke mechanism reproduces a broad range of experimental observations with good overall predictive capability. Explicit treatment of bath-gas–mixture effects leads to modest but systematic improvements in selected predictions within the validation conditions considered here.

Despite overall consistency among mechanisms for many observables, significant discrepancies remain, particularly for NO and N_2O formation and under H_2-rich, high-pressure conditions. Applying the Burke bath-gas–mixture treatment to only six reactions leads to limited but systematic changes under the conditions examined here; larger impacts are expected at pressures in which key reactions are in the fall-off region.

Overall, this work presents a reliable and predictive NH_3/H_2 combustion mechanism that explicitly incorporates bath-gas–mixture effects. Future efforts should extend this treatment to additional pressure-dependent reactions and reassess kinetic sensitivities once composition dependence is more comprehensively implemented. Given that neglecting bath-gas–mixture effects can introduce errors comparable to or exceeding those associated with pure-bath-gas rate coefficients, further progress will require treating both sources of uncertainty in a consistent framework.

Author contributions

Yu-Chi Kao: literature review, kinetic modeling, mechanism generation, writing and editing manuscript. Anna C. Doner: rate and thermochemistry calculations, writing original draft. Timo T. Pekkanen: master-equation rate calculations and writing manuscript. Chuangchuang Cao: literature review and kinetic modeling. Sunkyu Shin: kinetic modeling and editing manuscript. Alon Grinberg Dana: literature review, rate and thermochemistry calculations. Yi-Pei Li: funding acquisition and supervision. William H. Green: funding acquisition, supervision, and editing manuscript.

Conflicts of interest

There are no conflicts of interest to declare.

Data availability

All data supporting the findings of this study are available within the article and its supplementary information (SI). This includes computed potential energy surfaces, thermochemical parameters, pressure-dependent rate coefficients, and the complete kinetic mechanism files in both Cantera and Chemkin formats, as well as the corresponding RMG input files, Flexible Transition State Theory (FTST) files, and master-equation (ME) calculation outputs. Supplementary information is available. See DOI: https://doi.org/10.1039/d5cp04149j.

Additional input scripts used for mechanism generation, master-equation simulations, and kinetic analyses are available upon reasonable request from the corresponding author (Prof. William H. Green, whgreen@mit.edu).

References

1 A. Grinberg Dana, O. Elishav, A. Bardow, G. E. Shter and G. S. Grader, *Angew. Chem., Int. Ed.*, 2016, **55**, 8798–8805.
2 H. Kobayashi, A. Hayakawa, K. Somarathne and E. Okafor, *Proc. Combust. Inst.*, 2019, **37**, 109–133.
3 A. Valera-Medina, H. Xiao, M. Owen-Jones, W. I. F. David and P. J. Bowen, *Prog. Energy Combust. Sci.*, 2018, **69**, 63–102.
4 O. Herbinet, P. Bartocci and A. Grinberg Dana, *Fuel Commun.*, 2022, **11**, 100064.
5 M. Alnajideen, H. Shi, W. Northrop, D. Emberson, S. Kane, P. Czyzewski, M. Alnaeli, S. Mashruk, K. Rouwenhorst, C. Yu, S. Eckart and A. Valera-Medina, *Carbon Neutrality*, 2024, **3**, 13.

6422 | *Phys. Chem. Chem. Phys.*, 2026, **28**, 6411–6424

This journal is © the Owner Societies 2026

6 A. G. Szanthoffer, I. G. Zsély, L. Kawka, M. Papp and T. Turányi, *Appl. Energy Combust. Sci.*, 2023, **14**, 100127.

7 A. Grinberg Dana, K. Kaplan, M. Keslin, C. Cao and W. H. Green, *Energy Fuels*, 2024, **38**, 22482–22500.

8 M. Monge-Palacios, X. Zhang, N. Morlanes, H. Nakamura, G. Pezzella and S. M. Sarathy, *Prog. Energy Combust. Sci.*, 2024, **105**, 101177.

9 S. Girhe, A. Snackers, T. Lehmann, R. Langer, F. Loffredo, R. Glaznev, J. Beeckmann and H. Pitsch, *Combust. Flame*, 2024, **267**, 113560.

10 G. Huang, H. Wang, L. Tian, O. Haidn and N. Slavinskaya, *Fuel*, 2025, **400**, 135810.

11 M. P. Burke and R. Song, *Proc. Combust. Inst.*, 2017, **36**, 245–253.

12 L. Lei and M. P. Burke, *J. Phys. Chem. A*, 2019, **123**, 631–649.

13 P. J. Singal, J. Lee, L. Lei, R. L. Speth and M. P. Burke, *Proc. Combust. Inst.*, 2024, **40**, 105779.

14 A. Stagni and T. Dinelli, *Chem. Eng. J.*, 2025, **526**, 170737.

15 M. Liu, A. Grinberg Dana, M. S. Johnson, M. J. Goldman, A. Jocher, A. M. Payne, C. A. Grambow, K. Han, N. W. Yee, E. J. Mazeau, K. Blondal, R. H. West, C. F. Goldsmith and W. H. Green, *J. Chem. Inf. Model.*, 2021, **61**, 2686–2696.

16 M. S. Johnson, X. Dong, A. Grinberg Dana, Y. Chung, D. J. Farina, R. J. Gillis, M. Liu, N. W. Yee, K. Blondal, E. Mazeau, C. A. Grambow, A. M. Payne, K. A. Spiekermann, H.-W. Pang, C. F. Goldsmith, R. H. West and W. H. Green, *J. Chem. Inf. Model.*, 2022, **62**, 4906–4915.

17 K. Kaplan, M. Keslin and A. Grinberg Dana, *Phys. Chem. Chem. Phys.*, 2025, **27**, 14924–14935.

18 M. Keskin, K. Kaplan and A. Grinberg Dana, *Phys. Chem. Chem. Phys.*, 2025, **27**, 2680–2691.

19 A. Jasper, *Faraday Discuss.*, 2022, **238**, 68–86.

20 *Turbulent Combustion Modeling: Advances, New Trends and Perspectives*, ed. T. Echekki and E. Mastorakos, Springer, 2011.

21 N. Mitnik, S. Haba and A. Grinberg Dana, *Chem. Phys. Chem.*, 2022, **23**, e202200373.

22 A. Stagni, S. Arunthanayothin, M. Dehue, O. Herbinet, F. Battin-Leclerc, P. Bréquigny, C. Mounaïm-Rousselle and T. Faravelli, *Chem. Eng. J.*, 2023, **471**, 144577.

23 X. Zhang, S. P. Moosakutty, R. P. Rajan, M. Younes and S. M. Sarathy, *Combust. Flame*, 2021, **234**, 111653.

24 X. Zhang, K. K. Yalamanchi and S. Mani Sarathy, *Fuel*, 2023, **341**, 127676.

25 Y. Zhu, H. J. Curran, S. Girhe, Y. Murakami, H. Pitsch, K. Senecal, L. Yang and C.-W. Zhou, *Combust. Flame*, 2024, **260**, 113239.

26 F. Weigend and R. Ahlrichs, *Phys. Chem. Chem. Phys.*, 2005, **7**, 3297–3305.

27 J.-D. Chai and M. Head-Gordon, *Phys. Chem. Chem. Phys.*, 2008, **10**, 6615–6620.

28 T. H. Dunning, *J. Chem. Phys.*, 1989, **90**, 1007–1023.

29 H.-J. Werner, P. J. Knowles, G. Knizia, F. R. Manby and M. Schütz, *WIREs Comput. Mol. Sci.*, 2012, **2**, 242–253.

30 H.-J. Werner, P. J. Knowles, F. R. Manby, J. A. Black, K. Doll, A. Heßelmann, D. Kats, A. Köhn, T. Korona, D. A. Kreplin, Q. Ma, I. Miller, F. Thomas, A. Mitrushchenkov, K. A. Peterson, I. Polyak, G. Rauhut and M. Sibaev, *J. Chem. Phys.*, 2020, **152**, 144107.

31 H.-J. Werner, P. J. Knowles *et al.*, *MOLPRO, version, a package of ab initio programs*, see https://www.molpro.net.

32 M. J. Frisch, G. W. Trucks, H. B. Schlegel, G. E. Scuseria, M. A. Robb, J. R. Cheeseman, G. Scalmani, V. Barone, G. A. Petersson, H. Nakatsuji, X. Li, M. Caricato, A. V. Marenich, J. Bloino, B. G. Janesko, R. Gomperts, B. Mennucci, H. P. Hratchian, J. V. Ortiz, A. F. Izmaylov, J. L. Sonnenberg, D. Williams-Young, F. Ding, F. Lipparini, F. Egidi, J. Goings, B. Peng, A. Petrone, T. Henderson, D. Ranasinghe, V. G. Zakrzewski, J. Gao, N. Rega, G. Zheng, W. Liang, M. Hada, M. Ehara, K. Toyota, R. Fukuda, J. Hasegawa, M. Ishida, T. Nakajima, Y. Honda, O. Kitao, H. Nakai, T. Vreven, K. Throssell, J. A. Montgomery, Jr., J. E. Peralta, F. Ogliaro, M. J. Bearpark, J. J. Heyd, E. N. Brothers, K. N. Kudin, V. N. Staroverov, T. A. Keith, R. Kobayashi, J. Normand, K. Raghavachari, A. P. Rendell, J. C. Burant, S. S. Iyengar, J. Tomasi, M. Cossi, J. M. Millam, M. Klene, C. Adamo, R. Cammi, J. W. Ochterski, R. L. Martin, K. Morokuma, O. Farkas, J. B. Foresman and D. J. Fox, *Gaussian-16 Revision C.01*, 2016, Gaussian Inc., Wallingford CT.

33 F. Neese, *Wiley Interdiscip. Rev.: Comput. Mol. Sci.*, 2012, **2**, 73–78.

34 A. Grinberg Dana, D. Ranasinghe, H. Wu, C. Grambow, X. Dong, M. Johnson, M. Goldman, M. Liu and W. Green, *ARC - Automated Rate Calculator, version 1.1.0*, https://github.com/ReactionMechanismGenerator/ARC, 2019.

35 M. Kállay, P. R. Nagy, D. Mester, Z. Rolik, G. Samu, J. Csontos, J. Csóka, P. B. Szabó, L. Gyevi-Nagy, B. Hégely, I. Ladjánszki, L. Szegedy, B. Ladóczki, K. Petrov, M. Farkas, P. D. Mezei and Á. Ganyecz, *J. Chem. Phys.*, 2020, **152**, 074107.

36 MRCC, a quantum chemical program suite written by M. Kállay, P. R. Nagy, D. Mester, L. Gyevi-Nagy, J. Csóka, P. B. Szabó, Z. Rolik, G. Samu, J. Csontos, B. Hégely, Á. Ganyecz, I. Ladjánszki, L. Szegedy, B. Ladóczki, K. Petrov, M. Farkas, P. D. Mezei and R. A. Horváth. See https://www.mrcc.hu.

37 A. G. Dana, M. S. Johnson, J. W. Allen, S. Sharma, S. Raman, M. Liu, C. W. Gao, C. A. Grambow, M. J. Goldman, D. S. Ranasinghe, R. J. Gillis, A. M. Payne, Y.-P. Li, X. Dong, K. A. Spiekermann, H. Wu, E. E. Dames, Z. J. Buras, N. M. Vandewiele, N. W. Yee, S. S. Merchant, B. Buesser, C. A. Class, F. Goldsmith, R. H. West and W. H. Green, *Int. J. Chem. Kinet.*, 2023, **55**, 300–323.

38 D. R. Glowacki, C.-H. Liang, C. Morley, M. J. Pilling and S. H. Robertson, *J. Phys. Chem. A*, 2012, **116**, 9545–9560.

39 J. Zheng, J. L. Bao, S. Zhang, J. C. Corchado, R. Meana-Pañeda, Y.-Y. Chuang, E. L. Coitiño, B. A. Ellingson and D. G. Truhlar, *Gaussrate 17-B*, 2017.

40 S. H. Robertson, D. M. Wardlaw and A. F. Wagner, *J. Chem. Phys.*, 2002, **117**, 593–605.

41 *RDKit: Open-source cheminformatics*, https://www.rdkit.org.

42 H. Wu, A. M. Payne, H.-W. Pang, A. Menon, C. A. Grambow, D. S. Ranasinghe, X. Dong, A. Grinberg Dana and W. H. Green, *J. Phys. Chem. A*, 2024, **128**, 4335–4352.

43 D. G. Goodwin, H. K. Moffat, I. Schoegl, R. L. Speth and B. W. Weber, *Cantera: An Object-oriented Software Toolkit for*

This journal is © the Owner Societies 2026

Phys. Chem. Chem. Phys., 2026, **28**, 6411–6424 | **6423**

Chemical Kinetics, Thermodynamics, and Transport Processes, 2024, Version 3.1.0.

44 S. Inomata and N. Washida, *J. Phys. Chem. A*, 1999, **103**, 5023–5031.

45 S. J. Klippenstein, C. R. Mulvihill and P. Glarborg, *J. Phys. Chem. A*, 2023, **127**, 8650–8662.

46 H. M. T. Nguyen, S. Zhang, J. Peeters, T. N. Truong and M. T. Nguyen, *Chem. Phys. Lett.*, 2004, **388**, 94–99.

47 D. L. Baulch, C. T. Bowman, C. J. Cobos, R. A. Cox, T. Just, J. A. Kerr, M. J. Pilling, D. Stocker, J. Troe, W. Tsang, R. W. Walker and J. Warnatz, *J. Phys. Chem. Ref. Data*, 2005, **34**, 757–1397.

48 H.-W. Pang, X. Dong, M. S. Johnson and W. H. Green, *J. Phys. Chem. A*, 2024, **128**, 2891–2907.

49 G. Yin, B. Xiao, H. Zhan, E. Hu and Z. Huang, *Combust. Flame*, 2023, **249**, 112617.

50 K. P. Shrestha, B. R. Giri, R. Pelé, K. Aljohani, P. Brequigny, F. Mauss, F. Halter, L. K. Huynh and C. Mounaïm-Rousselle, *Combust. Flame*, 2025, **274**, 113954.

51 O. Mathieu and E. L. Petersen, *Combust. Flame*, 2015, **162**, 554–570.

52 J. Chen, X. Jiang, X. Qin and Z. Huang, *Fuel*, 2021, **287**, 119563.

53 J. Pareja, H. J. Burbano and Y. Ogami, *Int. J. Hydrogen Energy*, 2010, **35**, 1812–1818.

54 K. Aung, M. Hassan and G. Faeth, *Combust. Flame*, 1997, **109**, 1–24.

55 O. Kwon and G. Faeth, *Combust. Flame*, 2001, **124**, 590–610.

56 M. P. Burke, Z. Chen, Y. Ju and F. L. Dryer, *Combust. Flame*, 2009, **156**, 771–779.

57 M. C. Krejci, O. Mathieu, A. J. Vissotski, S. Ravi, T. G. Sikes, E. L. Petersen, A. Kérmonès, W. Metcalfe and H. J. Curran, *J. Eng. Gas Turbines Power*, 2013, **135**, 021503.

58 P. D. Ronney, *Combust. Sci. Technol.*, 1988, **59**, 123–141.

59 U. Pfahl, M. Ross, J. Shepherd, K. Pasamehmetoglu and C. Unal, *Combust. Flame*, 2000, **123**, 140–158.

60 T. Jabbour and D. F. Clodic, *ASHRAE Trans.*, 2004, **110**, 522–533.

61 A. Hayakawa, T. Goto, R. Mimoto, Y. Arakawa, T. Kudo and H. Kobayashi, *Fuel*, 2015, **159**, 98–106.

62 K. Takizawa, A. Takahashi, K. Tokuhashi, S. Kondo and A. Sekiya, *J. Hazard. Mater.*, 2008, **155**, 144–152.

63 A. Ichikawa, A. Hayakawa, Y. Kitagawa, K. Kunkuma Amila Somarathne, T. Kudo and H. Kobayashi, *Int. J. Hydrogen Energy*, 2015, **40**, 9570–9578.

64 B. L. W. G. Yanchao Li and M. Bi, *Combust. Sci. Technol.*, 2018, **190**, 1804–1816.

65 B. Mei, X. Zhang, S. Ma, M. Cui, H. Guo, Z. Cao and Y. Li, *Combust. Flame*, 2019, **210**, 236–246.

66 X. Han, Z. Wang, M. Costa, Z. Sun, Y. He and K. Cen, *Combust. Flame*, 2019, **206**, 214–226.

67 K. P. Shrestha, C. Lhuillier, P. B. Amanda Alves Barbosa, F. Contino, C. Mounaïm-Rousselle, L. Seidel and F. Mauss, *Proc. Combust. Inst.*, 2021, **38**, 2163–2174.

68 C. Lhuillier, P. Brequigny, N. Lamoureux, F. Contino and C. Mounaïm-Rousselle, *Fuel*, 2020, **263**, 116653.

69 S. Xu, Z. Liu, H. Chen, Y. Chao and L. Xu, *Processes*, 2025, **13**, 466.

70 K. N. Osipova, X. Zhang, S. M. Sarathy, O. P. Korobeinichev and A. G. Shmakov, *Fuel*, 2022, **310**, 122202.

71 A. Stagni, C. Cavallotti, S. Arunthanayothin, Y. Song, O. Herbinet, F. Battin-Leclerc and T. Faravelli, *React. Chem. Eng.*, 2020, **5**, 696–711.

6424 | *Phys. Chem. Chem. Phys.*, 2026, **28**, 6411–6424

This journal is © the Owner Societies 2026